JOURNAL OF MATERIALS SCIENCE 39 (2004) 7199–7205

# Predicting freckle formation in single crystal Ni-base superalloys

S. TIN
*Department of Materials Science and Metallurgy, University of Cambridge, Pembroke St., Cambridge CB2 3QZ, UK*
*E-mail: st298@hermes.cam.ac.uk*

T. M. POLLOCK
*Department of Materials Science and Engineering, University of Michigan, 2300 Hayward St., Ann Arbor, MI 48109, USA*

Freckle formation has been investigated in thirty-two distinct experimental single crystal Ni-base superalloys with large compositional variations. In addition to variations in alloy chemistry, the components studied in this investigation consisted of cylindrical bars with different diameters and solid blade-shaped components unidirectionally solidified in industrial casting trials. The occurrence of freckles was statistically assessed in over four hundred and seventy single crystal components. Detailed analyses of the microstructures, segregation behavior and phase transformation temperatures are presented and utilized to develop regression models capable of predicting the occurrence of freckle formation during solidification. The significance of the physical parameters incorporated with the model, and the implication of the model on the approach for alloy design are discussed.
© *2004 Kluwer Academic Publishers*

## 1. Introduction

Single crystal Ni-base superalloy components are critical to the operation of advanced gas turbine engines for both power generation and aerospace applications. Used extensively in the hot section of turbine engines, single crystal Ni-base superalloys exhibit a unique combination of physical and mechanical properties that enable these materials to sustain significant loads at high temperatures in corrosive environments with minimal deformation or degradation. Over the past forty years, development of both advanced processing technologies and alloys have enabled modern gas turbine engines to operate at temperatures in excess of 1600 K to achieve large efficiency gains and increased power output. Although these single crystal components have inherently desirable properties to begin with, increasingly high levels of refractory elements have been alloyed with the Ni-base material to further enhance high temperature creep properties.

As the complexity and alloying content of these advanced high refractory content Ni-base superalloys increases, difficulties associated with manufacture and processing of single crystal components requires consideration. Tungsten and rhenium additions serve as potent solid-solution strengtheners in Ni-base superalloys and consequently extend the temperature capability of the alloy [1–3]. These constituent refractory elements, however, also contribute to the formation of macroscopic grain defects, such as freckle chains and misoriented grains. During unidirectional solidification in conventional Bridgman furnaces, micro-segregation allows for the accumulation of solute within the dendritic mushy zone. With solidification oriented antiparallel to the direction of gravity, the compositional changes associated with solute segregation in the dendritic mushy zone results in a density imbalance between the bulk liquid and the segregated solute. Due to preferential partitioning of tungsten and rhenium into the solid phase during solidification, the resultant buoyancy forces associated with the density difference between the comparatively less dense solute and the bulk liquid can initiate thermosolutal convection and cause grain defect formation during solidification.

Since the formation of macroscopic grain defects containing high angle boundaries is detrimental to the structural integrity of the cast component at elevated temperatures, large-scale manufacture of single crystal components for critical applications is quite challenging. Early efforts to prevent freckle formation included modification of gating designs and development of empirical defect maps [4] based on relationships between processing parameters, such as thermal gradient, G, and solidification or withdrawal rate, R. More recent studies pertaining to freckle formation have concentrated on the development of computational process models [5–9] and the incorporation of Rayleigh-based criterion to describe the onset of thermosolutal convection and the subsequent formation of grain defects [10–12]. However, the lack of published data has limited validation of these models over a broad range of composition

applicable to commercial and experimental multicomponent Ni-base superalloys. The coupling of thermodynamic databases with solidification models exhibits great potential, but caution should be exercised when applying these computational models to experimental alloy compositions outside the range where the thermodynamic models have been optimized. Nonetheless, these studies have contributed significantly to the understanding of the processes resulting in grain defect formation during directional solidification.

The breakdown of single crystal solidification in Ni-base superalloys can be attributed to both alloy composition and processing parameters. For a specific alloy composition, systematic variations in processing parameters revealed that a critical primary dendrite arm spacing, $\lambda_1$, exists below which the onset of thermosolutal convection is suppressed [13]. Additionally, studies designed to investigate the influence of alloy composition have identified tungsten, rhenium, tantalum and carbon additions to be statistically significant with respect the formation of freckle defects during solidification [14, 15]. Hence, similar to the Rayleigh analysis, the development of effective prediction criteria that can be used to assess the susceptibility of single crystal castings to form defects requires incorporation of both compositional and processing variables. In this study, neural networks were applied to assess the relative effects of individual variables on grain defect formation. Furthermore, detailed analyses of thirty-six distinct experimental single crystal alloy compositions unidirectionally solidified over a range of processing conditions were used to develop a physically-motivated semi-empirical model for prediction of freckle formation.

## 2. Experimental

A large number of experimental Ni-base single crystal alloys were analyzed to elucidate the influence of alloy composition on thermosolutal convection and freckle formation. Twenty distinct alloy compositions were solidified in large ceramic investment molds under constant processing conditions as solid blade-shaped components. An additional twenty-four casting trials were used to unidirectionally solidify twelve experimental alloys as cylindrical bars with varying diameters. In total, forty-four industrial casting trials were conducted and thirty-two distinct alloy compositions were investigated. Geometries of the cast components varied from blade-shaped castings to cylindrical bars with diameters of 12.7, 15.7 and 19.0 mm. Compositions of these experimental single crystal alloys are grouped in three separate alloy series: SX, ME and CE, Table I. Following solidification, all of the unidirectionally solidified castings were macroetched in a hot nitric bath to reveal the presence of high angle grain boundaries associated with freckle chains and misoriented grains. The number, location and size of the defects were statistically assessed for all of the experimental alloy compositions. With the solidification of seven blade shaped components or fourteen cylindrical bars per casting trial, four hundred and seventy castings were analyzed over the course of the investigation.

TABLE I Nominal compositions of the experimental single crystal Ni-based alloys (wt.%)

| Alloy | Al | Cr | Co | Hf | Re | Ta | W | Mo | C | Ni |
|---|---|---|---|---|---|---|---|---|---|---|
| SX-1 | 6.0 | 4.5 | 12.5 | 0.16 | 6.3 | 7.0 | 5.8 | 0.0 | 0.05 | Bal. |
| SX-2 | 6.1 | 4.5 | 12.5 | 0.15 | 6.5 | 9.0 | 5.8 | 0.0 | – | Bal. |
| SX-3 | 5.7 | 4.0 | 11.5 | 0.12 | 5.0 | 6.0 | 5.0 | 0.0 | – | Bal. |
| SX-4 | 5.7 | 5.0 | 13.5 | 0.12 | 5.0 | 6.0 | 6.5 | 0.5 | – | Bal. |
| SX-5 | 6.3 | 4.0 | 13.5 | 0.18 | 6.5 | 6.0 | 5.0 | 0.0 | – | Bal. |
| SX-6 | 6.3 | 5.0 | 11.5 | 0.18 | 6.5 | 6.0 | 6.5 | 0.5 | – | Bal. |
| SX-7 | 6.3 | 5.0 | 11.5 | 0.12 | 5.0 | 9.0 | 5.0 | 0.0 | – | Bal. |
| SX-8 | 6.3 | 4.0 | 13.5 | 0.12 | 5.0 | 9.0 | 6.5 | 0.5 | – | Bal. |
| SX-9 | 5.7 | 5.0 | 13.5 | 0.18 | 6.5 | 9.0 | 5.0 | 0.0 | – | Bal. |
| SX-10 | 5.7 | 4.0 | 11.5 | 0.18 | 6.5 | 9.0 | 6.5 | 0.5 | – | Bal. |
| SX-11 | 6.1 | 4.5 | 12.5 | 0.15 | 5.0 | 9.0 | 5.8 | 0.0 | 0.10 | Bal. |
| SX-12 | 6.1 | 4.5 | 12.5 | 0.15 | 6.5 | 9.0 | 5.8 | 0.0 | 0.10 | Bal. |
| SX-13 | 6.3 | 5.0 | 13.5 | 0.18 | 5.0 | 6.0 | 5.0 | 0.5 | 0.10 | Bal. |
| SX-14 | 6.3 | 4.0 | 11.5 | 0.18 | 5.0 | 6.0 | 6.5 | 0.0 | 0.10 | Bal. |
| SX-15 | 5.7 | 5.0 | 11.5 | 0.12 | 6.5 | 6.0 | 5.0 | 0.5 | 0.10 | Bal. |
| SX-16 | 5.7 | 4.0 | 13.5 | 0.12 | 6.5 | 6.0 | 6.5 | 0.0 | 0.10 | Bal. |
| SX-17 | 5.7 | 4.0 | 13.5 | 0.18 | 5.0 | 9.0 | 5.0 | 0.5 | 0.10 | Bal. |
| SX-18 | 5.7 | 5.0 | 11.5 | 0.18 | 5.0 | 9.0 | 6.5 | 0.0 | 0.10 | Bal. |
| SX-19 | 6.3 | 4.0 | 11.5 | 0.12 | 6.5 | 9.0 | 5.0 | 0.5 | 0.10 | Bal. |
| ME-1 | 6.8 | 7.0 | 7.5 | 0.14 | 4.6 | 6.1 | 2.4 | 1.5 | 0.00 | Bal. |
| ME-2 | 6.7 | 7.0 | 7.5 | 0.14 | 4.6 | 6.1 | 2.3 | 1.5 | 0.00 | Bal. |
| ME-3 | 6.7 | 7.0 | 7.5 | 0.13 | 1.4 | 6.0 | 7.3 | 1.5 | 0.00 | Bal. |
| ME-4 | 6.7 | 7.0 | 7.5 | 0.14 | 1.4 | 6.1 | 7.2 | 1.5 | 0.00 | Bal. |
| ME-5 | 4.4 | 7.0 | 7.5 | 0.12 | 4.4 | 6.0 | 7.2 | 1.5 | 0.00 | Bal. |
| ME-6 | 4.4 | 7.0 | 7.5 | 0.13 | 4.5 | 6.0 | 7.1 | 1.5 | 0.00 | Bal. |
| ME-7 | 4.8 | 7.0 | 7.5 | 0.14 | 1.5 | 6.4 | 2.5 | 1.5 | 0.00 | Bal. |
| ME-8 | 4.9 | 7.0 | 7.5 | 0.14 | 1.5 | 6.5 | 2.5 | 1.5 | 0.00 | Bal. |
| ME-9 | 6.5 | 7.0 | 7.5 | 0.14 | 4.5 | 5.8 | 7.0 | 1.5 | 0.13 | Bal. |
| ME-10 | 6.4 | 7.0 | 7.5 | 0.14 | 4.4 | 5.8 | 7.0 | 1.5 | 0.12 | Bal. |
| ME-11 | 4.6 | 7.0 | 7.5 | 0.14 | 1.4 | 6.2 | 7.4 | 1.5 | 0.13 | Bal. |
| ME-12 | 4.5 | 7.0 | 7.5 | 0.14 | 1.4 | 6.1 | 7.4 | 1.5 | 0.13 | Bal. |
| ME-13 | 4.6 | 7.0 | 7.5 | 0.14 | 4.7 | 6.2 | 2.4 | 1.5 | 0.13 | Bal. |
| ME-14 | 4.7 | 7.0 | 7.5 | 0.15 | 4.8 | 6.2 | 2.4 | 1.5 | 0.13 | Bal. |
| ME-15 | 7.1 | 7.0 | 7.5 | 0.15 | 1.5 | 6.2 | 2.4 | 1.5 | 0.14 | Bal. |
| ME-16 | 7.0 | 7.0 | 7.5 | 0.14 | 1.4 | 6.2 | 2.4 | 1.5 | 0.13 | Bal. |
| CE-1 | 5.6 | 7.0 | 7.5 | 0.00 | 2.8 | 8.4 | 4.5 | 1.5 | 0.00 | Bal. |
| CE-2 | 5.5 | 7.0 | 7.5 | 0.00 | 2.8 | 8.1 | 4.3 | 1.5 | 0.00 | Bal. |
| CE-3 | 5.8 | 7.0 | 7.5 | 0.28 | 2.9 | 4.0 | 4.6 | 1.5 | 0.00 | Bal. |
| CE-4 | 5.8 | 7.0 | 7.5 | 0.31 | 3.1 | 3.9 | 4.7 | 1.5 | 0.00 | Bal. |
| CE-5 | 5.8 | 7.0 | 7.5 | 0.00 | 3.0 | 3.9 | 4.8 | 1.5 | 0.14 | Bal. |
| CE-6 | 5.8 | 7.0 | 7.5 | 0.00 | 3.0 | 4.0 | 4.8 | 1.5 | 0.14 | Bal. |
| CE-7 | 5.5 | 7.0 | 7.5 | 0.27 | 2.8 | 8.2 | 4.5 | 1.5 | 0.13 | Bal. |
| CE-8 | 5.4 | 7.0 | 7.5 | 0.26 | 2.9 | 8.4 | 4.5 | 1.5 | 0.12 | Bal. |

Constituent phases associated with the as-cast microstructure of each alloy composition were carefully analyzed using both optical and electron microscopy. Temperatures corresponding to the phase transformations of the constituent phases in the experimental alloys, including solidus and liquidus temperatures, were measured using a SETSYS 18 Differential Thermal Analysis (DTA) unit. Finally, a modified-Scheil analysis was used to characterize the partitioning behaviour of the various alloying elements in the experimental alloys. Additional details of the experimental materials and procedure can be found in previous investigations by Tin and Pollock [14, 15].

## 3. Results

Microstructural analyses of the as-cast single crystals revealed heavily segregated dendritic microstructures in both the blade-shaped components and the cylindrical bars, Fig. 1. The dendritic microstructures

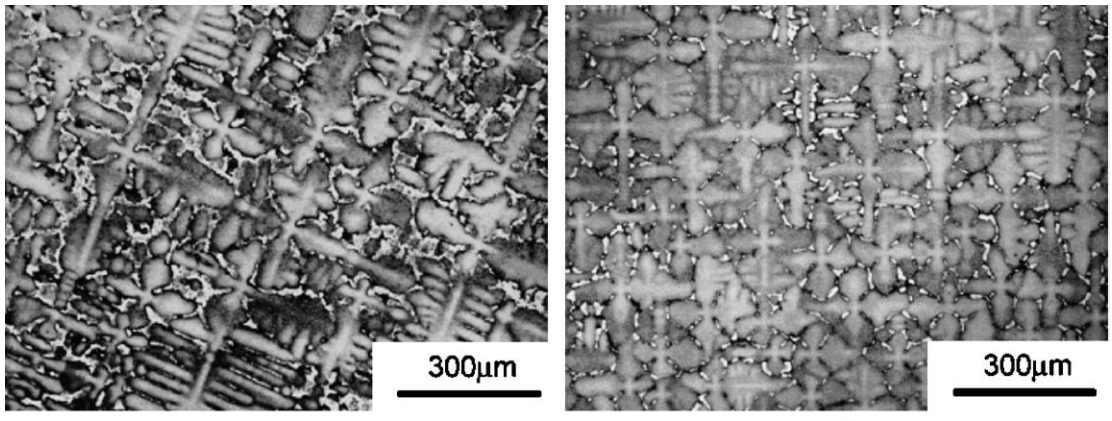


*Figure 1* Micrographs of the as-cast dendritic microstructures corresponding to: (a) blade-shaped components and (b) bar-shaped components.

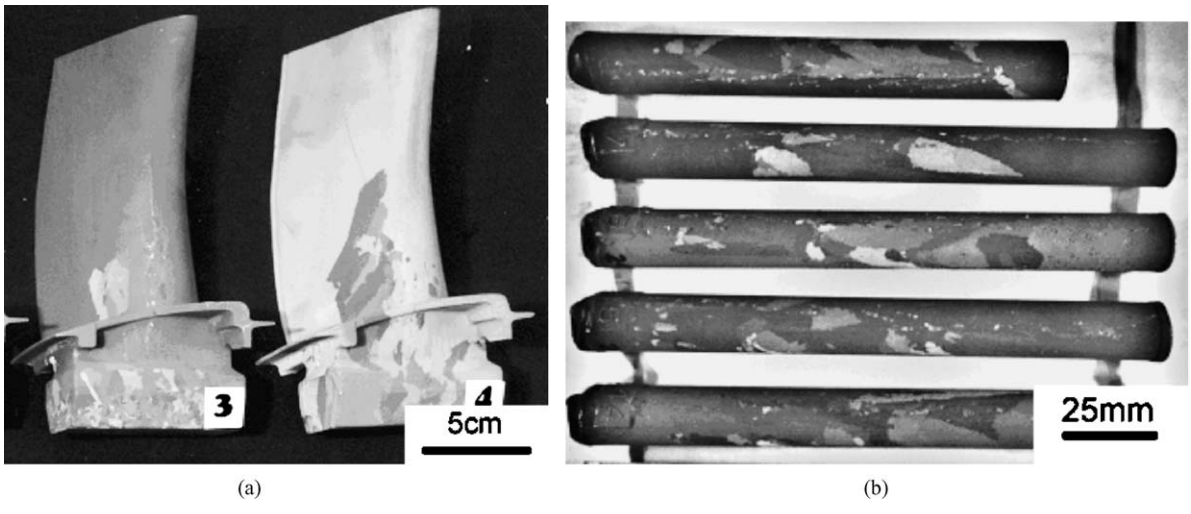


*Figure 2* Micrographs revealing macroscopic grain defects on the surface of directionally solidified: (a) blades and (b) bars.

corresponding to the blade and bar-shaped components appeared quite similar and are reflected in the corresponding primary dendrite arm spacings, $\lambda_1$. Corresponding spacings were measured to be 410, 340, 400 and 460 $\mu$m, respectively for the blade-shaped components and the cylindrical bars (12.7, 15.7 and 19.0 mm diameter). Microstructures were comprised primarily of $\gamma'$ precipitates distributed within a $\gamma$ matrix. Contained within the interdendritic regions of a large number of alloys were large pools of $\gamma$–$\gamma'$ eutectic. Various Ta-rich MC carbides were also observed to reside within the interdendritic regions of alloys containing intentional additions of carbon, Fig. 1.

Formation of macroscopic grain defects, such as freckle chains and misoriented grains, on the surfaces of the various castings can be seen in Fig. 2. After assessing the character of defects for each of the castings, a statistical average was taken for each distinct alloy composition and processing condition. Freckling results for the three alloy series are summarized in Fig. 3. Previous analyses revealed variations in tungsten, rhenium, tantalum and carbon levels are statistically significant factors with respect to the formation of freckle defects [14, 15]. Tungsten and rhenium additions induce freckle formation while tantalum and carbon additions tend to suppress the processes leading up to the formation of freckles. Variations in the levels of cobalt, chromium, molybdenum and hafnium were determined to be insensitive to macroscopic grain defect formation during solidification.

The segregation characteristics of the constituent elements in the experimental single crystal compositions were assessed using a modified Scheil analysis [14–16]. The refractory elements, rhenium, tungsten and tantalum were determined to exhibit the largest degree of segregation during solidification. Tantalum tended to partition preferentially to the solute, while tungsten and rhenium were revealed to segregate preferentially to the solid phases during solidification. A compilation of experimentally measured distribution coefficients, $k$, are listed in Table II. The magnitude of the coefficients corresponds to the degree of segregation during solidification. Since the partition coefficient is defined as $k = C_S/C_L$, where $C_S$ is the composition of the solid phase and $C_L$ is the composition of the liquid phase, measured values of $k$ greater or less than unity correspond to preferential segregation to the solid phase or liquid phase, respectively.

Results from the DTA were used to reveal the influence of alloy composition on solidus and liquidus temperatures for these experimental single crystals,

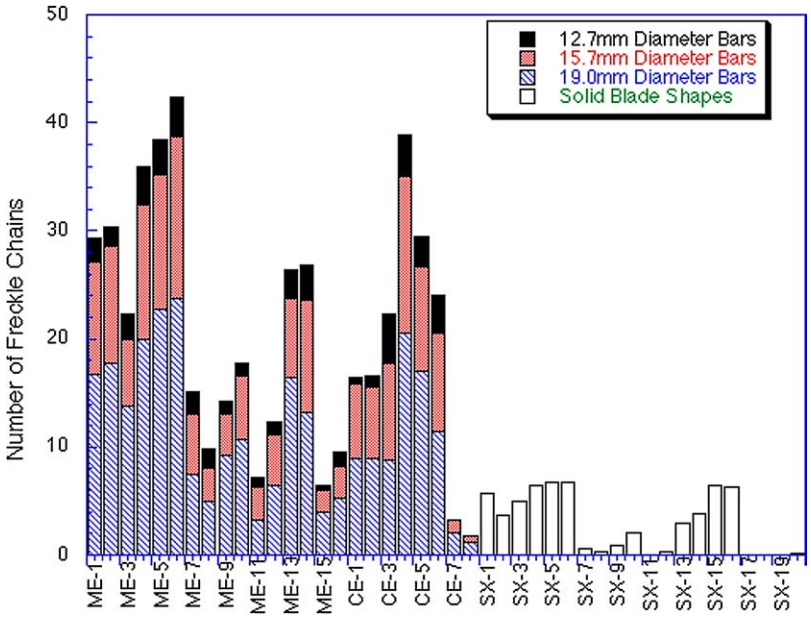


*Figure 3* Number of freckle chains observed on the surface of the various cast components.

Table III. The thermal measurements also indicated precipitation of the Ta-rich MC carbides occurred as part of a eutectic reaction between the corresponding solidus and liquidus temperature of the alloy. Consistent with a temperature invariant phase transformation, the eutectic MC carbide temperatures were much less sensitive to shifts in composition than the solidus and liquidus temperatures. Over the wide range of alloy composition investigated, the majority of the carbide eutectic temperatures were reported to occur at ~1386°C (1659 K). Unlike the solidus and liquidus temperatures that varied from 1381–1436°C and 1342–1371°C, respectively, all of the measured eutectic MC carbide temperatures fell within the relatively small range of 1377–1393°C for all three sets of alloys. Although the $\gamma'$ solvus temperatures were determined from alloys in the as-cast condition and are not the true equilibrium values, these temperatures provide extremely useful information when determining parameters for solution heat-treatments.

TABLE II Average fitted distribution coefficients for the experimental Ni-based alloys

| | Al | Cr | Co | Ni | Ta | W | Re | Mo |
|---|---|---|---|---|---|---|---|---|
| SX-1 | 0.85 | 1.06 | 1.06 | 0.96 | 0.74 | 1.39 | 1.39 | – |
| SX-2 | 0.81 | 1.16 | 1.08 | 0.94 | 0.69 | 1.54 | 1.60 | – |
| SX-3 | 0.89 | 1.08 | 1.05 | 0.95 | 0.79 | 1.54 | 1.43 | – |
| SX-6 | 0.87 | 1.07 | 1.07 | 0.95 | 0.80 | 1.42 | 1.38 | 1.40 |
| SX-9 | 0.87 | 1.12 | 1.07 | 0.95 | 0.77 | 1.54 | 1.43 | – |
| SX-10 | 0.84 | 1.17 | 1.10 | 0.94 | 0.74 | 1.42 | 1.41 | – |
| SX-11 | 0.87 | 1.11 | 1.09 | 0.93 | 0.72 | 1.44 | 1.39 | – |
| SX-12 | 0.86 | 1.13 | 1.13 | 0.95 | 0.80 | 1.38 | 1.49 | – |
| SX-13 | 0.88 | 1.05 | 1.05 | 0.96 | 0.88 | 1.39 | 1.42 | 1.46 |
| SX-16 | 0.90 | 1.06 | 1.03 | 0.95 | 0.89 | 1.36 | 1.33 | – |
| SX-19 | 0.88 | 1.12 | 1.06 | 0.95 | 0.83 | 1.44 | 1.36 | 1.35 |
| SX-20 | 0.87 | 1.13 | 1.08 | 0.93 | 0.76 | 1.39 | 1.41 | – |
| ME-2 | 0.92 | 1.13 | 1.07 | 0.97 | 0.78 | 1.54 | 1.37 | 1.23 |
| ME-4 | 0.92 | 1.15 | 1.09 | 0.96 | 0.76 | 1.36 | 1.38 | 1.25 |
| ME-6 | 0.89 | 1.07 | 1.05 | 0.96 | 0.79 | 1.38 | 1.35 | 1.20 |
| ME-7 | 0.94 | 1.07 | 1.05 | 0.98 | 0.78 | 1.58 | 1.25 | 1.13 |
| ME-10 | 0.89 | 1.15 | 1.09 | 0.94 | 0.87 | 1.31 | 1.30 | 1.27 |
| ME-11 | 0.92 | 1.06 | 1.04 | 0.98 | 0.89 | 1.28 | 1.28 | 1.20 |
| ME-14 | 0.95 | 1.06 | 1.04 | 0.97 | 0.89 | 1.35 | 1.30 | 1.18 |
| ME-15 | 0.95 | 1.13 | 1.09 | 0.98 | 0.84 | 1.40 | 1.23 | 1.24 |
| CE-1 | 0.85 | 1.15 | 1.10 | 0.97 | 0.72 | 1.39 | 1.42 | 1.30 |
| CE-4 | 0.89 | 1.12 | 1.10 | 0.97 | 0.67 | 1.39 | 1.39 | 1.25 |
| CE-5 | 0.88 | 1.13 | 1.08 | 0.98 | 0.76 | 1.25 | 1.39 | 1.28 |
| CE-8 | 0.86 | 1.15 | 1.10 | 0.97 | 0.77 | 1.35 | 1.34 | 1.30 |

### 3.1. Physically based linear regression model

During conventional directional solidification processes, the onset of thermosolutal convection corresponds with the ratio of the buoyancy forces and surrounding frictional forces, similar to the Rayleigh analysis. Since the solutal density inversion scales accordingly with the buoyancy forces, the magnitude of the driving force resulting in fluid flow can be estimated using the measured partitioning coefficients and relations describing liquid densities as a function of composition. Densities of the bulk liquid and solute were estimated using the relationships reported by Sung and Poirier for measuring liquid densities of similar Ni-base superalloys [17]. Frictional forces, on the other hand, are proportional to the morphology of the mushy zone and resulting primary dendrite arm spacings. With knowledge of these parameters, linear regression can be applied to develop simple empirical relations between freckle formation, alloy composition and mushy zone morphology. For the non-carbon containing ME and CE series of alloys, which exhibited variations in both alloy chemistry and primary dendrite arm spacings (due to varying bar diameters) the relation can be written as follows:

$$\Phi = -41.4 + 400\left(\frac{\Delta\rho}{\rho}\right) + 31.7\left(\frac{\lambda_1}{\lambda^*}\right) \qquad (1)$$

where $\Phi$ is the number of freckle defects, $\Delta\rho/\rho$ is the normalized density difference between the solute and

TABLE III Solidus, liquidus, carbide eutectic and $\gamma'$ solvus temperatures of the experimental Ni-based alloys

| | $T_S$ (solidus)°C | $T_{MC}$ (carbide)°C | $T_L$ (liquidus)°C | $\gamma'$ (solvus)°C |
|---|---|---|---|---|
| SX-1 | 1352 | – | 1412 | 1238 |
| SX-2 | 1340 | – | 1405 | 1263 |
| SX-3 | 1393 | – | 1436 | 1248 |
| SX-4 | 1376 | – | 1420 | 1223 |
| SX-5 | 1379 | – | 1429 | 1234 |
| SX-6 | 1333 | – | 1411 | 1244 |
| SX-7 | 1333 | – | 1401 | 1273 |
| SX-8 | 1337 | – | 1397 | 1275 |
| SX-9 | 1331 | – | 1407 | 1244 |
| SX-10 | 1336 | – | 1406 | 1267 |
| SX-11 | 1360 | 1386 | 1396 | 1264 |
| SX-12 | 1338 | 1390 | 1399 | 1240 |
| SX-13 | 1361 | 1383 | 1398 | 1231 |
| SX-14 | 1367 | 1390 | 1406 | 1246 |
| SX-15 | 1368 | 1388 | 1412 | 1212 |
| SX-16 | 1371 | 1391 | 1413 | 1246 |
| SX-17 | 1364 | 1386 | 1397 | 1248 |
| SX-18 | 1359 | 1386 | 1393 | 1254 |
| SX-19 | 1364 | 1386 | 1386 | 1272 |
| SX-20 | 1340 | 1377 | 1383 | 1260 |
| ME-1 | 1335 | – | 1397 | 1317 |
| ME-2 | 1333 | – | 1396 | 1312 |
| ME-3 | 1331 | – | 1393 | 1308 |
| ME-4 | 1331 | – | 1393 | 1305 |
| ME-5 | 1393 | – | 1426 | 1237 |
| ME-6 | 1396 | – | 1428 | 1260 |
| ME-7 | 1390 | – | 1416 | 1246 |
| ME-8 | 1391 | – | 1417 | 1242 |
| ME-9 | 1355 | 1383 | 1390 | 1305 |
| ME-10 | 1354 | 1378 | 1389 | 1305 |
| ME-11 | 1376 | 1391 | 1412 | 1222 |
| ME-12 | 1378 | 1391 | 1412 | 1220 |
| ME-13 | 1378 | 1393 | 1416 | 1207 |
| ME-14 | 1379 | 1393 | 1415 | 1209 |
| ME-15 | 1355 | 1377 | 1381 | 1300 |
| ME-16 | 1358 | 1378 | 1384 | 1297 |
| CE-1 | 1369 | – | 1402 | 1321 |
| CE-2 | 1370 | – | 1403 | 1322 |
| CE-3 | 1381 | – | 1416 | 1272 |
| CE-4 | 1379 | – | 1416 | 1266 |
| CE-5 | 1371 | 1385 | 1409 | 1237 |
| CE-6 | 1370 | 1385 | 1410 | 1239 |
| CE-7 | 1366 | 1386 | 1393 | 1291 |
| CE-8 | 1364 | 1385 | 1393 | 1294 |

the bulk liquid, $\lambda_1$ is the observed primary dendrite arm spacing in microns, and $\lambda^*$ corresponds to the critical dendrite arm spacing for SX-1 [13] (317 $\mu$m). With constant component geometries and resulting primary dendrite arm spacings for the SX series of experiments, the magnitude of the buoyancy force was the only significant parameter resulting in freckle formation in the non-carbon containing alloys. Therefore:

$$\Phi = -1.7 + 171\left(\frac{\Delta\rho}{\rho}\right) \tag{2}$$

Carbide precipitation in these experimental alloys was identified to have a significant beneficial influence in preventing the formation of freckles during solidification. Consequently, the carbon-containing alloys in the SX, ME and CE series of experiments were considered separately. Carbon containing alloys in the ME and CE series were regressed to follow:

$$\Phi = -25.6 + 119\left(\frac{\Delta\rho}{\rho}\right) + 17.97\left(\frac{\lambda_1}{\lambda^*}\right) + 573.7\left(\frac{T_L - T_{MC}}{T_{Ni}}\right) \tag{3}$$

while the corresponding relationship for the carbon-bearing alloys in the SX series was:

$$\Phi = -17.6 + 451\left(\frac{\Delta\rho}{\rho}\right) + 573.7\left(\frac{T_L - T_{MC}}{T_{Ni}}\right) \tag{4}$$

where $T_L$ and $T_{MC}$ are the liquidus and carbide eutectic temperatures, respectively, and $T_{Ni}$ is the melting point of pure Ni (1728 K). Significantly fewer freckles were observed in alloys which precipitation of the carbides was measured to occur close to the liquidus ($T_L - T_{MC} < 11$°C). Application of these relationships for compositions within the range of alloys investigated show that the model was reasonably accurate in predicting the actual number of freckle defects forming on the surfaces of the castings for a wide range of alloys and process conditions, Fig. 4. Possibly due to the geometrical constraints associated with the complex blade-shaped casting geometry of the SX alloys, the CE and ME alloys displayed better agreement between the actual and predicted number of defects.

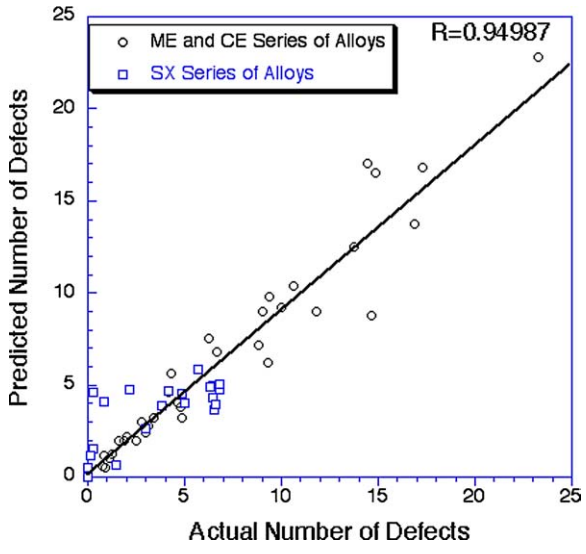


*Figure 4* Correlation between the actual and predicted number of freckle defects using the linear regression models.

## 4. Discussion

Development of new single crystal alloy compositions with enhanced high temperature creep properties requires a detailed understanding of how compositional changes influence aspects such as solidification processing and solution heat treatment. Although tungsten, rhenium and tantalum are effective strengtheners and improve the mechanical properties of the alloy, the overall content of these additions must be carefully balanced to optimize physical and mechanical properties

with commercial production requirements. The present investigation has focused on the development of models capable of predicting the susceptibility of experimental alloys to freckle formation as a function of both composition and processing parameters.

During unidirectional solidification, the onset of thermosolutal convection and the subsequent formation of freckle defects occur when the driving force for fluid flow exceeds the surrounding frictional forces. Hence, the occurrence of freckles can be expressed as a function of two competing forces. The de-stabilizing term is proportional to the magnitude of the buoyancy forces associated with the solute-induced density inversion ($\Delta\rho/\rho$), while the stabilizing term is closely related to the frictional parameter associated with the morphology of the mushy zone. The solidification parameters, thermal gradient ($G$) and solidification rate ($R$) govern the morphology of the mushy zone and are related to the resultant primary dendrite arm spacings [18], $G^{-1/2} \times R^{-1/4} \propto \lambda_1$. Furthermore, the precipitation of carbides within the mushy zone was also observed to suppress freckle formation. Thus, the term representing the retarding frictional force is expressed as a function of both $\lambda_1$ and a carbide precipitation term. Linear regression equations incorporating these parameters, Equations 1 to 4, were demonstrated to provide a reasonably accurate correlation with the occurrence of freckle defects, Fig. 4.

Most conventional single crystal Ni-base superalloys exhibit an inherent tendency to form convective instabilities during unidirectional solidification. The multicomponent nature of these alloys results in severe dendritic segregation of tungsten and rhenium into the solid phase during solidification that depletes the solute of dense refractory elements and increases the magnitude of the buoyancy forces. Conventional approaches taken to improve the solidification characteristics of these alloys have concentrated on tantalum additions that offset depleted levels of tungsten and rhenium in the solute by segregating preferentially into the liquid, thereby minimizing the density inversion. Results from this investigation clearly show that better understanding the complex interactions occurring within these industrially pertinent alloys and exploiting these effects can also enhance the intrinsic solidification characteristics. For example, aluminum additions have been typically associated with freckle formation [19, 20] in Ni-base superalloys. The present models, however, tend to indicate that in certain alloys elevated levels of aluminum can actually prevent the onset of thermosolutal convection. Due to its low density and characteristic partitioning behavior, aluminum additions contribute directly to the development of the density inversion in the mushy zone. Indirectly, aluminum additions decrease the liquidus temperature of the alloy, Table III. With solidus temperatures typically defined by the invariant temperatures associated with the pools of $\gamma - \gamma'$ eutectic, changes in liquidus temperatures influence the freezing range of the alloy and the resulting mushy zone morphologies, Equations 3 and 4. Although the primary dendrite arm spacings were unaffected, these morphological changes in the mushy zone suppress freckle formation and are consistent with previous statistical analysis from alloys in the ME and CE series [14]. Minor additions of carbon also improve the solidification characteristics of Ni-base superalloys. In addition to precipitating out as carbides during solidification, carbon additions to Ni-base superalloys have been demonstrated to minimize dendritic segregation by altering the partitioning characteristics of the constituent elements [14, 15]. Both of these effects associated with carbon additions inhibit the formation of freckle chains.

As the design requirements for high-temperature structural materials in gas turbine engines become increasingly demanding, the utilization of advanced materials and alloy compositions is required to achieve the desired performance and efficiency gains. Optimization of gas turbines for aerospace, power generation and marine applications has created a need for specialty alloys with different attributes due to various design criteria and constraints governing each application. Due to the high costs associated with the materials development, experimental alloys are typically developed under laboratory conditions and optimized using thermodynamic and mechanistic property-prediction algorithms with little consideration of the difficulties associated with the commercialization of the manufacturing process. Development of an effective model capable of predicting the occurrence of freckles during casting can greatly assist in the evaluation of experimental alloy compositions. In summary, the model presented in this study contributes significantly to the understanding the various complex elemental interactions in multicomponent Ni-base superalloys and is critical for the development of alloys optimized for both properties and processing.

## 5. Conclusions

(1) The onset of thermosolutal convection and the formation of freckles during unidirectional solidification are sensitive to both changes in primary dendrite arm spacing and alloy composition.

(2) The occurrence of freckle on single crystal castings can be effectively expressed as parameters relating the magnitude of the buoyancy forces and the morphology of the dendritic mushy zone.

(3) Grain defect formation during unidirectional solidification can be suppressed by exploiting the complex interactions occurring within these multicomponent alloys.

## References

1. G. L. ERICKSON, in "Superalloys 1996" (Warrendale, PA, TMS, 1996) p. 35.
2. A. F. GIAMEI and D. L. ANTON, *Metall. Trans.* **16A** (1985) 1997.
3. W. S. WALSTON, K. S. O'HARA, E. W. ROSS, T. M. POLLOCK and W. H. MURPHY, in "Superalloys 1996" (Warrendale, PA, TMS, 1996) p. 27.
4. J. S. TU and R. K. FORAN, *JOM* **44**(6) (1992) 26.
5. K. O. YU, J. J. NICHOLS and M. ROBINSON, *ibid.* **44**(6) (1992) 21.
6. K. O. YU, J. A. OTI, M. ROBINSON and R. G. CARLSON, in "Superalloys 1992" (Warrendale, PA, TMS, 1996) p. 135.

7. M. C. SCHNEIDER, J. P. GU, C. BECKERMANN, W. J. BOETTINGER and U. R. KATTNER, *Metall. Trans.* **28A** (1997) 1517.
8. S. D. FELICELLI, D. R. POIRIER and J. C. HEINRICH, *Journal of Crystal Growth* **177** (1997) 145.
9. *Idem.*, *Metall. Mater. Trans.* **29B** (1998) 847.
10. P. AUBURTIN, T. WANG, S. L. COCKCROFT and A. MITCHELL, *ibid.* **31B** (2000) 801.
11. C. BECKERMANN, J. P. GU and W. J. BOETTINGER, *ibid.* **31A** (2000) 2545.
12. W. YANG, W. CHEN, K. M. CHANG, S. MANNAN and J. DEBARBADILLO, *ibid.* **32A** (2001) 397.
13. T. M. POLLOCK and W. H. MURPHY, *ibid.* **27A** (1996) 1081.
14. S. TIN, T. M. POLLOCK and W. T. KING, in "Superalloys 2000" (Warrendale, PA, TMS, 2000) p. 201.
15. S. TIN, T. M. POLLOCK and W. MURPHY, *Metall. Mater. Trans.* **32A** (2001) 1743.
16. M. N. GUNGOR, *Metall. Trans.* **20A** (1989) 2529.
17. P. K. SUNG, D. R. POIRIER and E. McBRIDE, *Mater. Sci. Eng.* **A231** (1997) 189.
18. W. KURZ and D. J. FISHER, "Fundamentals of Solidification," 3rd ed. (Trans Tech Publications Ltd. Aedermannsdorf, Switzerland, 1992) p. 289.
19. A. F. GIAMEI and B. H. KEAR, *Metall. Trans.* **1** (1970) 2185.
20. S. M. COPLEY, A. F. GIAMEI, S. M. JOHNSON and M. F. HORNBECKER, *ibid.* **1** (1970) 2193.

*Received 10 March*
*and accepted 20 May 2004*